arXiv:1704.08266v1 [astro-ph.GA] 26 Apr 2017

Submitted to ApJ

Suzaku Measurements of Hot Halo Emission at Outskirts for Two Poor Galaxy Groups: NGC 3402 and NGC 5129

Jenna M. Nugent[1], Xinyu Dai[1], Ming Sun[2]

ABSTRACT

We present *Suzaku* off-center observations of two poor galaxy groups, NGC 3402 and NGC 5129, with temperatures below 1 keV. Through spectral decomposition, we measure their surface brightnesses and temperatures out to 330 and 680 times the critical density of the universe for NGC 3402 and NGC 5129, respectively. These quantities are consistent with extrapolations from existing inner measurements of the two groups. With the refined X-ray luminosities, both groups prefer L_X–T relations without a break in the group regime. Furthermore, we measure the electron number densities and hydrostatic masses at these radii. We find that the electron number density profiles require three β model components, with nearly flat slopes in the 3$^{\rm rd}$ β component for both groups. However, we find the effective slope in the outskirts to be $\beta_{out} = 0.59$ and 0.49 for NGC 3402 and NGC 5129, respectively. Adding the gas mass measured from the X-ray data and stellar mass from group galaxy members, we measure baryon fractions of $f_b = 0.113 \pm 0.013$ and 0.091 ± 0.006 for NGC 3402 and NGC 5129, respectively. Combining other poor groups with well measured X-ray emission to the outskirts, we find an average baryon fraction of $f_{b,ave} = 0.100 \pm 0.004$ for X-ray bright groups with temperatures between 0.8–1.3 keV, extending existing constraints to lower mass systems.

Subject headings: galaxies: groups: general — galaxies: groups: individual (NGC 3402, NGC 5129) — X-rays: galaxies: clusters — (cosmology:) large-scale structure of universe

[1]Homer L. Dodge Department of Physics and Astronomy, University of Oklahoma, Norman, OK 73019, jenugent@ou.edu

[2]University of Alabama in Huntsville, Huntsville, AL 35899

1. Introduction

Galaxy clusters and groups are virialized over-density regions in the universe. Based on numerical or semi-analytical simulations (e.g., Bryan & Norman 1998), the over-density of clusters and groups in the virial radius, r_{vir}, is 100 times the critical density of the universe for the prevailing concordance cosmology. However, observationally, we are more easily able to probe the central regions within $\sim r_{2500}$, which limits us from understanding the overall properties of these objects, such as their virial masses, temperatures and gas and stellar contents. Therefore, measuring cluster and group properties at their outskirts close to the virial radius becomes a major endeavor. For galaxy clusters, successful measurements of the X-ray emission near r_{200} have been made with *Suzaku* for many individual clusters (Fujita et al. 2008; Bautz et al. 2009; George et al. 2009; Reiprich et al. 2009; Kawaharada et al. 2010; Hoshino et al. 2010; Simionescu et al. 2011; Akamatsu et al. 2011; Sato et al. 2012; Walker et al. 2012; Ichikawa et al. 2013) and by using stacking analysis (Dai et al. 2007; Rykoff et al. 2008; Shen et al. 2008; Dai et al. 2010; Eckert et al. 2012). Yet for galaxy groups, it is more difficult to study the X-ray emission at large radii because of the relatively weaker emission. The situation is especially severe for poor groups with temperatures below $T \lesssim 1$ keV, where only measurements from stacking analysis exists for these groups (Dai et al. 2007; Anderson et al. 2015).

Galaxy groups are important to study the properties of virialized structures, especially to test the deviations from self-similar model predictions, such as the L_X–T relation. More accurate measurements in the group regime will extend the mass range for these tests. They are also important to better quantify the missing baryon problem in the low-redshift universe (Bregman 2007, and references therein), in which the observed amount of baryons is less than that determined based on the cosmic microwave background observed from the early universe. While observations of nearby galaxies yielded only about 10% of the expected baryon content (Persic & Salucci 1992; Bristow & Phillipps 1994; Fukugita et al. 1998), observations of rich galaxy clusters with $T > 5$ keV retain the cosmological value after adjusting for stellar mass (Vikhlinin et al. 2006). Illustrated by Figure 11 in the Discussion, we can see that the observed baryon fraction of nearby systems as a function of gravitational potential well (represented here by total mass within the radius at which the average mass density is 200 times the critical density of the universe, r_{200}) follows a broken power-law model (Dai et al. 2010, 2012). The data for all but the most massive objects fall below the cosmological fraction measured at high redshift. The group regime is arguably the transition region, where the baryon loss becomes significant. However, we lack sufficient data to accurately determine the mass threshold of the baryon loss, because of the difficulties in accurately measuring their properties, especially to their outskirts. These missing baryons are theorized to be in a warm-hot intergalactic medium, which permeates the large scale

structure filaments of the universe, and the hot gas haloes of galaxy clusters and groups. Although this general picture is likely correct, some key questions still remain ambiguous, such as whether virialized regions of group masses retain their baryons and whether the missing baryons of galaxies fall in the virialized regions of their parent groups. Answering these questions will guide the development of numerical simulations with non-gravitational processes such as feedback and pre-heating (e.g., Benson 2010).

In this paper, we observe the diffuse, extended emission from two poor galaxy groups in the soft X-ray band with *Suzaku*, which is best for such observations due to its low, stable background resulting from its low-earth orbit. The two groups studied in this paper, and many of their properties, are well documented in the literature. For instance, NGC 3402 Group, also called SS2b153, NGC 3411 Group and USGC S152, was analyzed in Mahdavi et al. (2005) as a group of about 5 members, which appears to be perfectly round, containing "no evidence of irregularity". This nearby ($z = 0.0153$) fossil group has a global temperature[1], $kT = 0.88 \pm 0.04$ keV (Sun et al. 2009). Although NGC 5129 Group has nearly the same global temperature as NGC 3402 Group, $kT = 0.90 \pm 0.04$ keV, (Sun et al. 2009), it is a nearby ($z = 0.0230$) loose group with $N_{gal} \sim 19$ (Mahdavi & Geller 2004). Hence, both groups lie in the temperature range that so far has a dearth of successful measurements. Throughout this paper, we adopt the 3-year WMAP cosmology and a flat universe: $H_0 = 73$ km s^{-1} Mpc^{-1}, $\Omega_m = 0.26$ and $\Omega_\Lambda = 0.74$.

2. Observations and Data Reduction

We observed the poor fossil group, NGC 3402 Group (hereafter NGC 3402), centered at 22.1 arcmin (r_{420}) away from the group center with the position angle (PA) of 108° in the X-ray band using *Suzaku* on 2010 December 27 for 49 ks. Also with *Suzaku*, we observed the poor galaxy group, NGC 5129 Group (hereafter NGC 5129), using two off-center pointings with separations from the group center of 16.2 and 15.3 arcmin (larger at r_{300}) on 2010 December 18 with PAs of 78° and 161° and exposure times of 55 ks and 38 ks, respectively. Additionally, to better model the background, we performed one background pointing for each galaxy group at $2.3r_{200}$ and $2.4r_{200}$ for NGC 3402 and NGC 5129, respectively. The two background observations were carried out within 10 days of the corresponding target observations. All five observations were done using the three remaining X-ray Imaging Spectrometers (XISs) onboard *Suzaku*: two front-illuminated (FI) CCDS (XIS0 and XIS3)

[1]These global temperatures have been adjusted for the significant change in AtomDB, as discussed in Section 4.3.

and one back-illuminated (BI) CCD (XIS1). Details of these observations are listed in Table 1. Also, ROSAT images of each group are depicted in Figure 1, where the radial extent of the *Chandra* analysis from Sun et al. (2009), the extent of r_{500} based on the electron number density profiles discussed later in the paper, *Suzaku* FOV for the group and background observations are shown. From this, we can see that each group pointing lies beyond r_{500} and a significant area of NGC 5129 is analyzed here, due to its two spatially separate pointings.

The data were reduced using the software package *HEAsoft* version 6.13. We first reprocessed the data using the FTOOL `aepipeline`, which also performs default screening, along with the XIS calibration database (20120210). All data were reduced according to *The Suzaku Data Reduction Guide*[2]. Additionally, we excluded times when the revised cut-off rigidity value (COR2) was less than 6 GV to improve the signal-to-noise (S/N) ratio by reducing instances of background flaring.

Then we removed the resolved foreground and background X-ray sources, as well as the ^{55}Fe calibration sources located at two corners of each detector (Figure 2). The locations of the calibration sources were known, and the remaining sources were excised by visual inspection. Furthermore, most likely due to a micro-meteorite impact, a strip of the XIS0 detector (located at DETX = 70–150) was deemed unusable by the XIS team[3]. Following their notes for reducing XIS0 data after the anomaly[4], we used a C-shell script to generate a region to remove all events in the affected area and formed a region to remove possible spurious sources near this strip. We applied this to the XIS0 CCDs for all observations. For example, Figure 2 illustrates these sources and their regions for the XIS0 3x3 and 5x5 combined NGC 3402, 5129 1$^{\rm st}$ and 5129 2$^{\rm nd}$ observations. We then examined the light curves using `Xselect` for instances of background flaring in the 0.5–5 keV band after the above screening processes, and we found no significant background flares in all observations.

3. Surface Brightness

We employed two methods to measure the mean surface brightness (SB) for each target. First is the direct subtraction method, since we have background observations at greater than $2r_{200}$ performed within 10 days of each target observation enabling us to measure the

[2]http://heasarc.gsfc.nasa.gov/docs/suzaku/analysis/abc/abc.html

[3]http://www.astro.isas.ac.jp/suzaku/doc/suzakumemo/suzakumemo-2010-01.pdf

[4]http://www.astro.isas.jaxa.jp/suzaku/analysis/xis/xis0_area_discriminaion

NXB background well. In this method, the SB is computed for both the target and the corresponding background observations and the net value is the difference between the two. The second method involves modeling the spectra of both the target and the background, and the surface brightness is determined from the best-fit model parameters for the group emission.

3.1. Direct Subtraction Method

Using version 2.4b of `Xselect`, we read in both the 3x3 and 5x5 event files with the COR2 > 6 GV screening for each CCD and extracted the total events for each observation in the 0.6–1.3 keV energy range, excluding the resolved X-ray, calibration and anomalous sources mentioned in Section 2. Then we calculated the mean surface brightnesses for both the group and background pointings. Since the group emission is extended and much larger than the PSFs of XIS, the net SB is just the subtraction of the two. For uncertainties, we only considered Poisson noise. Table 2 lists these net surface brightness values. We did not detect any group emission from this crude analysis.

3.2. Spectral Analysis

Spectra of each observation were generated using `Xselect`, and we binned all spectra with a minimum of 25 photons in each bin using the FTOOL `GRPPHA`. We generated the instrumental response by generating redistribution matrix files (RMFs) using the XIS response generator `xisrmfgen` ver. 2012-04-21. Next, we used the Monte Carlo ray-tracing algorithm `xissimarfgen` ver. 2010-11-05 to produce the ancilliary response files (ARFs), which account for the instrument's effective area. The input GTI files were from the cleaned event files with the COR2 condition applied. Finally, we approximated emission caused by cosmic ray interactions by making the non-X-ray background (NXB) spectra using the tool `xisnxbgen` ver. 2010-08-22, which uses the night-Earth data collected by *Suzaku* (Yamaguchi et al. 2006). Night-Earth data were accumulated for more than 750 ks for the BI CCD and 1.5 Ms for the FI CCDs, combined. Since XIS0 and XIS3 are both front-illuminated CCDs, we were able to combine their spectra, NXB and response files using `addascaspec`. To avoid systematic uncertainties in the background calibration, we fit all spectra in the energy ranges: 0.6–7 keV for FI CCDs and 0.5–5 keV for the BI CCD (Ichikawa et al. 2013). We modeled all spectra with `Xspec` ver. 12.8.0, and fit the FI and BI spectra simultaneously to improve the constraints on model parameters.

The spectra of the two background observations were modeled by several components: NXB, Galactic emission, unresolved extragalactic sources and emission due to solar wind charge exchange (SWCX) (Fujimoto et al. 2007). The NXB component is subtracted from the spectra using our pre-generated NXB spectra. To address any possible shortcomings in the NXB generated by `xisnxbgen`, we visually inspected the NXB subtracted binned and unbinned spectra for any significant NXB excess, and added Gaussian lines to model the residual NXB emission lines. Adapted from Yamaguchi et al. (2006), Table 3 provides the emission lines and their energies, and all normalizations were allowed to fit freely during the spectral fits. Thus, the NXB subtracted background model is: *wabs*(pow + apec[0.2] + apec[0.07] + apec[0.4]*(for NGC 5129 only)*) + gau*(residual NXB lines). The unresolved extragalactic sources were modeled using a power-law (*pow*) component with photon index (Γ) frozen at 1.41 (Humphrey & Buote 2006). Referencing the model parameters in Humphrey et al. (2011, 2012), we accounted for Galactic X-ray emission with two absorbed *apec* models ($kT = 0.07$ keV and $kT = 0.2$ keV, fixed). Since NGC 5129 is close to the North Polar Spur, we added a third Galactic *apec* component at $kT = 0.4$ keV (Gastaldello et al. 2007; Sun et al. 2009). We used zero redshift and solar abundances for the background *apec* models, where the temperatures of these models are fixed during the spectral analysis. The Galactic and extragalactic components are modified by Galactic absorption (Dickey & Lockman 1990). We performed simultaneous fits between the FI and BI spectra, since the Galactic, extragalactic and galaxy group emission should correspond between different CCDs. However, the residual NXB line normalizations were allowed to fit independently due to the variability of this type of emission between differing CCDs, as well as in time. We obtained acceptable fits to the background spectra, and Table 4 lists the best-fit parameters. The reduced χ^2, $\chi^2_{min}/dof \approx 1$, suggesting that we have successfully modeled the background.

Furthermore, we considered the possibility of systematic uncertainties in the background spectral models. To do this, we fit all combinations of models where: $\Gamma = 1.41$ or 1.56, the Galactic foreground *apec* temperature would be one single component and allowed to vary, or frozen at two components ($kT = 0.07$ keV and 0.2 keV), and residual NXB would be added or not considered. For NGC 5129, we kept the additional fixed $kT = 0.4$ keV *apec* component for all models. The resulting models were all comparatively good fits, varying little in reduced χ^2 (see Table 4). The average best fit temperatures for the galactic foreground in the single *apec* background models were $kT_{ave} = 0.17$ keV and 0.19 keV, for NGC 3402 and NGC 5129, respectively.

We modeled the group halo plasma emission using an *apec* model modified by Galactic absorption, allowing the temperatures to vary freely and with the remaining parameters frozen at $Z = 0.2Z_{\odot}$ and the respective redshift of each group's central galaxy ($z = 0.0153$ for NGC 3402 and $z = 0.0230$ for NGC 5129). Here we have used the default abundance table

for this version of `Xspec`, *angr* (Anders & Grevesse 1989). This group emission was added to all the background components to model the target group spectra. For the normalizations of Galactic and extragalactic background models, we constrained them to be within the 1σ uncertainties from best-fit values of the corresponding normalizations determined from the background spectra. All eight of the different background models were applied to the source group spectra in this way, producing eight corresponding group spectral models. We chose the models shown in Tables 4 and 5 due to their overall excellent fit to the data (including consideration of residuals) and being the models nearest to mean and median across all three group spectra, when distributed by temperature. The variations in reduced χ^2 for the group models are also quite small (see Table 5). Figure 3 shows the best fit unfolded models with individual model components of each group and background observation with spectral data overlayed. Our chosen model's parameters and best-fit normalizations are given in Tables 4 and 5, in which NXB emission line parameters and normalizations are left out for compactness.

Also included in Table 5 are the systematic uncertainties (σ_{syst}) introduced from the background model for the group *apec* temperature and normalization. While the σ_{syst} in the group temperature is overall negligible compared to statistical, the σ_{syst} in the normalization is more significant. Furthermore, we changed the fixed abundance from $Z = 0.2Z_{\odot}$ to $Z = 0.33Z_{\odot}$ solely in the chosen group models and re-fit. The change in group temperature between models with these abundances is small, $\Delta kT = 0.01$ keV for all three group observations. However, the relative change in group normalization between models is larger, $\Delta norm/norm = 0.30$, 0.30 and 0.23 for NGC 3402, NGC 5129 1$^{\rm st}$ and NGC 5129 2$^{\rm nd}$, respectively. Ultimately, we chose to perform all subsequent analyses and computations solely considering statistical uncertainties. In addition, we averaged the uncertainties in group normalization shown in Table 5, when performing ensuing calculations. Since we have successfully isolated different components in the target spectra through spectral modeling, this allows us to better detect the group emission compared to the direct subtraction method. We detected the group emission at 13.4σ, 4.4σ, and 2.8σ for NGC 3402, NGC 5129 1$^{\rm st}$, and NGC 5129 2$^{\rm nd}$, respectively, and we use these constraints on the group emission from the spectral modeling in the subsequent analysis.

Due to the faintness of our detected signal, it is important to consider contributions from the galaxy group core smeared by the PSF into the CCD field-of-view. We estimate this scattered emission by considering both the PSF and off-axis effective area of *Suzaku*. Using the plots from the *Suzaku Technical Description* (TD), we first approximate the level of emission from the core due to the PSF that we should expect for our observations. Extrapolating the *Suzaku* PSF (Figure 6.12 of the TD) to our observation radii, we find that the smeared emission from the core at these radii is between five and six orders of magnitude

less than that of the group center, for both galaxy groups. We also include the effects of vignetting, which reduces this signal further. Following the plot for 1.49 keV in Figure 6.17 of the TD, the effective area is ∼1000 times less at the group cores since they are off-axis in the observations. Combining these, we find the contribution from scattered light to be approximately four and five orders of magnitude below our detected signal, for NGC 3402 and NGC 5129, respectively. Since the scattering emission from the group core is several orders of magnitude below the detected signal for both groups, it is negligible to our subsequent analysis.

Solar wind charge exchange (SWCX) (Fujimoto et al. 2007) provides additional non-X-ray background to the spectra. Similar to the residual NXB, SWCX can be modeled with Gaussian lines. Initially, we added these spectral lines to the models, allowing only the normalizations to be free. However, this only marginally improved the fits in some cases and, in many other cases, caused `Xspec` to fall into local minima. This can be attributed to the large number of free parameters when including SWCX lines. Visually, there seem to be no contributions from SWCX in the spectra, albeit a few lines are nearly degenerate with the residual NXB lines. In addition, the spectra are well fit by the models excluding these lines, further indicating their inclusion an over-parameterization of the models. Considering these factors, we chose to simplify the models and exclude contributions from solar wind charge exchange.

4. Radial Profiles

4.1. AtomDB

The release of AtomDB ver. 2.0 in 2011, caused significant changes in the derived spectral properties of plasma with $kT < 2$ keV, due to updates in the Fe L-shell data (e.g., Sun 2012). The major quantity affected for our analysis is the gas temperature, which increases by 10–20% from ver. 1.3 to 2.0 and later versions. To estimate the temperature change in the inner profile, we compared the projected *Chandra* temperature profile of NGC 3402 from Sun et al. (2009) (which used AtomDB ver. 1.3.1) to the *Chandra* data reprocessed with CIAO 4.6.1 and CALDB 4.6.2 (post AtomDB ver. 2.0, O'Sullivan, private communication). By determining the shift between temperature profiles and averaging them, we found that the temperature measurements increased by 19% between pre–AtomDB 2.0 and post–2.0 analyses. We applied this shift to the subsequent temperature and entropy profiles of the inner data, as well as the global temperatures for these objects, as mentioned in the Introduction. These adjusted temperatures are used repeatedly in our analyses.

4.2. Emission Weighted Radius

Since the output from the spectral analyses are weighted by emission, we also computed the corresponding radii for each observation. These emission weighted radii, r_{emw}, were calculated by summing over all distances between each pixel in the extraction region and the X–ray center of each galaxy group, multiplied by the surface brightnesses at those pixel locations. Then we divided by the sum of the SBs at those radii.

To obtain the SB function for the outskirts of each group, we fit the outer data of the SB profiles to a power-law, allowing the normalization and powerlaw index to be free. Here we included the SBs we obtained in this work at the central location of each observation. We chose the outer data such that the cut-off corresponded to the innermost extent of the observations without extraction regions applied: 200 kpc and 90 kpc for NGC 3402 and NGC 5129, respectively. Furthermore, we approximated a grid of pixels over the extraction region by generating a cleaned event file with the COR2 condition and extraction regions applied. Then, we selected the locations of all events with $kT > 2$ keV, effectively excluding the group halo emission. Since our observations are dominated by background emission, this results in a uniform grid of pixel locations. The event files used were from the XIS0 observations. Although the extraction regions change between CCDs, we felt this approximation was justified given the quality of the data. Taking into account all this, we obtained the emission weighted radii, $r_{emw} = 383$, 282 and 329 kpc for NGC 3402, NGC 5129 1$^{\rm st}$ and NGC 5129 2$^{\rm nd}$, respectively.

Finally, we computed a radial binsize based on the location within which 68% of the total emission for each observation is contained, centered on the mean, namely r_{emw}. Specifically, we computed the radius at which 16% of all emission within the extraction region was contained and set this as our lower bound. The upper bound was found using the corresponding location within which 84% of emission is contained. We have overlayed these binsizes for all radial profiles, Figures 4 through 9.

4.3. Gas Temperature

In Figure 4, we plot the projected temperature profiles of NGC 3402 and NGC 5129 to r_{330} and r_{680}, respectively, by combining our outer *Suzaku* data with the inner, adjusted *Chandra* data (Sun et al. 2009), where we have plotted the asymmetric uncertainties originally found through `Xspec` instead of the symmetrized ones used in all other related calculations. Furthermore, for NGC 3402, we plotted the projected temperature profile derived from *XMM-Newton* observations, using AtomDB ver. 3.0 and SAS 13.5 (O'Sullivan, private

communication), based on the work by O'Sullivan et al. (2007).

Comparing the *Chandra* and *XMM-Newton* profiles of NGC 3402, we can see an overall agreement between them, where both temperature profiles exhibit "wiggles" that match in radii. O'Sullivan et al. (2007) discussed the temperature dip at $\sim$ 10–40 kpc as the possible presence of a "cool core that has been partially re-heated by AGN activity", resulting in a region of warmer gas enclosed within a shell of cool gas. Both the *Chandra* and *XMM-Newton* data show declines in temperature at $R > 50$ kpc. Our *Suzaku* emission weighted temperature at 383 kpc, $kT = 1.01 \pm 0.05$ keV is significantly higher than the outer most *Chandra* and *XMM-Newton* data points, yet is consistent with the peaks of the two profiles at $R < 30$ kpc and $R \sim 50$ kpc.

We tested adjusting the parameters in our `Xspec` models to assess whether our choice of fixed parameters could have given such a result. First, with the extrapolations of O'Sullivan et al. (2007), Eckmiller et al. (2011) and Johnson et al. (2011), we decreased the metallicity of the hot halo gas, while keeping the other fixed parameters at their original values in our spectral fits. Additionally, we tried an increase in abundance, with $Z = 0.5Z_{\odot}$. For all four abundances we chose (0.05, 0.1, 0.33, and $0.5Z_{\odot}$), we obtained best-fit temperatures greater than $\sim$1 keV. Also, we tried our original model with only the neutral hydrogen column density changed from the value of Dickey & Lockman (1990) and set to the value computed by Eckmiller et al. (2011), 0.1016×10^{22} cm^{-2}. Similarly, we obtain kT = 0.961 $\pm$ 0.042 keV, consistent with our original finding. Therefore, we concluded that the high *Suzaku* temperature measurement for NGC 3402 is not caused by our preferred choice of parameter values in the spectral modeling.

In the case of NGC 5129, both our *Suzaku* temperature measurements from the 1$^{\rm st}$ and 2$^{\rm nd}$ observations are consistent with the outer most *Chandra* data point. Comparing between the two *Suzaku* measurements, they are also consistent within 1σ and follow the declining trend of the inner data, typical of a universal temperature profile (Vikhlinin et al. 2005).

4.4. Surface Brightness

We produced the mean surface brightness profiles in Figure 5, by combining our *Suzaku* measurements at r_{emw} and the inner data derived from the *Chandra* observations (Sun et al. 2009). We have converted the *Suzaku* count rates (CRs) into *Chandra* ACIS-S CRs using the online tool `WebPIMMS`. Our *Suzaku* data considerably expand the measurements on the surface brightness profiles, especially in the case of NGC 3402, in which the profile is extended by $\sim$125 kpc. The *Suzaku* SB measurements are lower than the inner SBs, as

expected, and fall on the declining trends established by the inner data, although for NGC 5129, there appear to be fluctuations in our data. However, they are consistent within 2σ of each other.

We estimated the total count rates of the two groups to greater than $0.88r_{500}$, by interpolating and integrating the SB profiles. Combining this with the adjusted global temperatures for these groups, $k\overline{T}_{3402} = 0.88$ keV and $k\overline{T}_{5129} = 0.90$ keV (Sun et al. 2009), we estimate the 0.5–2 keV unabsorbed X-ray flux as: $F_{X,3402} = (1.85 \pm 0.04) \times 10^{-11}$ erg cm^{-2} s^{-1} and $F_{X,5129} = (3.06 \pm 0.09) \times 10^{-12}$ erg cm^{-2} s^{-1}, and the 0.1–100 keV bolometric X-ray luminosities as: $L_{Xbol,3402} = (1.43 \pm 0.03) \times 10^{43}$ erg s^{-1} and $L_{Xbol,5129} = (5.40 \pm 0.17) \times 10^{42}$ erg s^{-1}. Also, we estimated the bolometric luminosities out to r_{500} and r_{200}. Furthermore, we found the X-ray luminosities in the ROSAT band (0.1–2.4 keV) to be: $L_{ROSAT,3402} = (1.38 \pm 0.03) \times 10^{43}$ erg s^{-1} and $L_{ROSAT,5129} = (5.20 \pm 0.16) \times 10^{42}$ erg s^{-1}. The aforementioned values can also be seen in Table 8.

4.5. Electron Number Density

The X-ray surface brightness at some projected distance on the sky, R, can be expressed in terms of the emission measure along the line of sight, $EM = \int n_e^2 \mathrm{d}l$ by

$$S = \int_{-\infty}^{\infty} n_e^2 \, \mathrm{d}l \; \frac{\Lambda(T,z)}{4\pi D_L^2}, \tag{1}$$

where $\Lambda(T,z)$ is the "emissivity in the considered energy band, taking into account the absorption by our galaxy, the redshift, and the instrumental response" (Arnaud 2005) and D_L is the luminosity distance. Converting to deprojected, three-dimensional radius r, we obtain

$$S(R) = 2 \int_R^{\infty} n_e^2(r) \, \frac{r\mathrm{d}r}{\sqrt{r^2 - R^2}} \frac{\Lambda(T,z)}{4\pi D_L^2}, \tag{2}$$

in which we compute D_L from the group redshift and $\Lambda(T,z)$ from the `Xspec` normalization and count rate,

$$k = \frac{10^{-14}}{4\pi[D_A(1+z)]^2} \int n_e n_H \mathrm{d}V \tag{3}$$

$$CR = \int n_e^2 \mathrm{d}V \frac{\Lambda(T,z)}{4\pi D_L^2}, \tag{4}$$

where $n_e \approx 1.2 n_H$ since the ratio of the number of H to He is approximately 10% and most electrons come from H and He in these systems (Arnaud 2005). Combining these we get,

$$\Lambda(T,z) = \frac{CR}{k} \frac{10^{-14}(1+z)^2}{1.2}. \tag{5}$$

To calculate $n_e(r)$ from Equation 2, we needed to measure the projected surface brightness $S(R)$ and the shape of the $n_e(r)$ profile. In this paper, $S(R)$ was measured from our *Suzaku* data through the spectral analysis, and the shape of the $n_e(r)$ profile was initially measured from the inner *Chandra* data (Sun et al. 2009), and then updated by adding the *Suzaku* data points.

We first used the inner *Chandra* data to measure the shape of the number density profiles for the two groups. Most galaxy clusters and groups' X-ray number densities and surface brightnesses can be well described by the class of models called β–models (Bregman 2007, and references therein). In the β–model, assuming spherical symmetry, the electron number density of the gas is parameterized by,

$$n_e(r) = n_{e0}\left(1+\left(\frac{r}{r_c}\right)^2\right)^{-3\beta/2}, \tag{6}$$

where n_{e0} is the value of n_e at $r = 0$, r_c is the core radius, β is the slope of the density profile typically observed to be ~ 0.5 for groups (Mulchaey 2000). Thus, by Equations 2 and 6, we get,

$$S(R) = S_0\left(1+\left(\frac{R}{r_c}\right)^2\right)^{-3\beta+1/2}, \tag{7}$$

This single β–Model form is sufficient for many rich clusters, but is overall a poor fit to the emission from groups (Mulchaey 2000). To test this, we began with the single β–model and fit to the *Chandra* number density profile for each group obtained by Sun et al. (2009). Though initially asymmetric, we symmetrized the uncertainties in the *Chandra* data by subtracting the higher bound by the lower bound and dividing by two. Unless otherwise stated, all uncertainties used in the calcluation of subsequent quantities and their errors have been symmetrized. Figure 6 depicts that the single β–Model is indeed not a good fit to the group data, especially at large radii where our observations take place. Therefore, we chose to use a two component β–model, or a 2β–Model, $n_e(r) = n_{e1}(n_{e01}, r, r_{c1}, \beta_1) + n_{e2}(n_{e02}, r, r_{c2}, \beta_2)$. The resultant fits were much improved, with $\chi^2_{min}/dof = 2.27/58$ and $2.08/46$ for NGC 3402 and 5129, respectively. However, with reduced χ^2 values so low ($\chi^2_{red} \approx 0.04$), it is apparent that the uncertainties have been overestimated. To remedy this, we decreased the uncertainties to $\sim 20\%$ their original value for each group, such that the $\chi^2_{min}/dof \approx 1$. Furthermore, we analyzed the normalized residuals of these models, which resulted in wavy, patterned residuals, as opposed to random ones indicative of a good fit. We conclude that the data is more complicated than the models used here. Fortunately, our analyses focus on the outskirts, so the effect of this complication is negligible.

Using the best-fit parameters from the 2β–model and their associated uncertainties

obtained from the inner density profiles, we inverted Equation 2 to calculate the de-projected electron number density at our *Suzaku* observations. Then, we re-fit the 2β–model to the density profiles with the outer *Suzaku* data included, yielding $\chi^2_{min}/dof = 196/60$ and $66.9/50$ for NGC 3402 and NGC 5129, respectively. Figure 7 shows that the 2β–model is not suitable for these data; while the inner radii are well fit, the outer *Suzaku* data illustrate that a flatter, third β–model is needed.

We thus added a third β–model component, and fixed $r_{c3} = 200$ kpc in our fitting procedure. We calculated χ^2_{min} for a grid of fixed β_3 values for the inner data. We then used the best fit parameters and the associated uncertainties to invert Equation 2 and calculate the de-projected number densities for the *Suzaku* data. With these outer *Suzaku* n_e included, we performed χ^2 minimization again for each fixed β_3 value. During the χ^2 minimization processes, we noticed there was switching occurring between models. Specifically, instead of the third β–model being the flat component needed to better fit the outer data, the first or second β–models were being preferred. Alleviating this required the addition of prior terms to the χ^2. These were chosen such that χ^2 would return a large value if the first and second β–Model parameters varied more than the 3σ relative uncertainties in parameters from the 2β–Model fits to the inner data. Including these priors, we obtained preliminary estimates of $\beta_3 = -0.14 \pm 0.03$ for NGC 3402 and $\beta_3 = -0.11 \pm 0.05$ for NGC 5129.

Using these priors, we took the best-fit parameters, their uncertainty ranges and relative uncertainties in the n_e at the r_{emw} as preliminary estimates. At this point, we used brute force uncertainty estimation, where we computed the χ^2 over an 8-dimensional grid of parameter values, based on their aforementioned initial estimates and the resultant $n_e(r_{emw})$. Then we computed corresponding likelihoods and obtained probabilities, which were binned by $n_e(r_{emw})$, giving us our probability distribution with respect to $n_e(r_{emw})$. The mean $n_e(r_{emw})$ were chosen to be the n_e associated with the global minimum χ^2 for the full grid. The 1σ uncertainties in $n_e(r_{emw})$ were found by taking the 68% area under the probability distributions, centered on the mean $n_e(r_{emw})$, in that these mean n_e were off-peak. For NGC 3402, this worked very well. However, NGC 5129 was more complicated since this mean n_e matched with the peaks of the distributions. In this case, at least one mean n_e was located such that the upper uncertainty was unbound. To remedy this, we chose the median n_e (or 50% area under the probability distribution) to replace the mean n_e, then calculated the 1σ uncertainties as for NGC 3402.

Also, we obtained model parameters and their 1σ uncertainties by finding $\Delta\chi^2$ for each parameter's range of values and then fit a quadratic to each to find the parameter values where $\Delta\chi^2 = 1$. Table 7 provides relative 1σ uncertainties in n_e and best-fit parameters with 1σ uncertainties for inner and outer data with priors in the χ^2 to prevent switching

between β–models. Figure 8 shows the best-fit 3β–Model electron number density profiles. Compared to Figure 7, the electron number densities derived from the *Suzaku* data are lower, and the 3β–Model is indeed a much better fit to the data. The requirement for negative (or nearly negative) β_3, leading to a flatter profile in the outskirts (especially for NGC 3402) illustrates the presence of additional gas at these large radii. To quantify this, we computed the slopes of each profile beyond 100 kpc, where the n_e could be characterized by a single β–Model. We obtained $\beta_{out} \approx 0.59$ and 0.49 for NGC 3402 and NGC 5129, respectively.

To obtain the total number density of the hot gas, we assume $n\mu = n_e\mu_e$, where μ is the mean molecular weight and μ_e is the mean molecular weight per free electron. Assuming total ionization, $n_e \approx 1.2n_H$ and $\mu \approx 0.62$, $\mu_e \approx \left(X + \frac{1}{2}(Y + Z)\right)^{-1} \approx 1.18$ in which $X = 0.7$, $Y = 0.29$ and the metallicity is $Z = 0.2Z_\odot = 0.004$.

4.6. Entropy

The entropy of the intragroup medium (IGM) is given by $K = T/n_e^{2/3}$, where T is in keV. Taking into account the overall temperature increase of 19% due to the change in AtomDB, we applied this to the entropy profiles of both groups, as seen in Figure 9. Also plotted are the data determined from the analysis for the outskirts from this work, where we have used the symmetric uncertainties in the outer n_e and T to compute the uncertainty in entropy. There appears to be no tendency for the entropy in NCG 3402 to drop off or flatten in the outskirts, the latter of which has been observed in clusters (e.g, George et al. 2009; Hoshino et al. 2010; Kawaharada et al. 2010). In fact, our data indicate the opposite may be occuring, although with the uncertainties in the outskirts, this finding is inconclusive. For NGC 5129, we can see with the contribution from both pointings that the outer entropy appears to be consistent with the trend of the inner data, with no indication of flattening. Furthermore, we have included in Figure 9 the self-similar models ($K \propto r^{1.1}$, Wong et al. 2016). Also plotted are power-law fits to the data, including the contributions from this work. The best fit power-law index, Γ, for NGC 3402 was $\Gamma = 0.94$, whereas for NGC 5129, the index was the much flatter $\Gamma = 0.59$.

5. Mass Determination

5.1. Hot Gaseous Halo and Stellar Masses

The gas mass density can be given by $\rho_{gas}(r) = m_p\mu_e n_e(r)$, where m_p is the mass of a proton. Assuming spherical symmetry, we can calculate the total gas mass enclosed by radius

r using the 3β–Model parameters to the emission weighted radii of our *Suzaku* observations for each galaxy group. Here we have used the same grid of parameter values and method used to derive the $n_e(r_{emw})$ for NGC 3402 in Section 4.5. Ultimately, the gas mass for NGC 3402 was $M_{gas,3402} = (1.03 \pm 0.03) \times 10^{12} M_\odot$ and $M_{gas,5129} = (8.28 \pm 0.11) \times 10^{11} M_\odot$ for NGC 5129.

To estimate the stellar mass component of each group, we chose to use the 2MASS K_s-band apparent magnitude of each member galaxy, since emission in the near-infrared (NIR) is less affected by interstellar extinction and the stellar mass-to-light (M/L) ratios in this band vary relatively little over a large range of star formation histories (Bell & de Jong 2001; Bell et al. 2003). To determine the galactic membership for each group, we implemented the SIMBAD Astronomical Database to obtain papers analyzing group membership. For NGC 5129, Mahdavi & Geller (2004) found 19 member galaxies out of $N_{obs} = 33$ total galaxies in the observation field. However, NGC 3402 was unique in that there are two differing sets of galaxies considered to be possible group members: 6 from Crook et al. (2007) and 4 from Guzzo et al. (2009). Two of these galaxies overlap, one being the brightest group galaxy, NGC 3402, resulting in 8 different member candidates. Using the most current radial velocity data from each paper, we further narrowed down the membership criteria using a redshift cutoff based on the velocity dispersion of the groups. To obtain the velocity dispersion, σ_{disp}, we used the scaling relation for groups and clusters, $\sigma_{disp} = 309$ km s^{-1} $(T/1 \text{ keV})^{0.64}$ (Xue & Wu 2000), where T is the global temperature adjusted for AtomDB as stated in the Introduction. Subsequently, we got $\sigma_{disp,3402} = 285$ km s^{-1} and $\sigma_{disp,5129} = 289$ km s^{-1}.

Constraining each galaxy to be within twice that dispersion of the cluster redshift, we were left with $N_{3402,czcut} = 5$ and $N_{5129,czcut} = 19$, consistent with the findings in Mahdavi et al. (2005) and Mahdavi & Geller (2004), respectively. Furthermore, to be consistent with the other mass measurements, we restricted the membership criteria such that each galaxy must lie within r_{emw}. This resulted in $N_{3402} = 4$ and $N_{5129} = 5$. After this, we used a stellar K_s mass-to-light ratio of $\Upsilon = 0.9$, in which we used a 30% 1σ uncertainty inferred from Figure 18 in Bell et al. (2003). Thus, the uncertainty of the mean is $0.3\Upsilon/\sqrt{N}$, where N is the number of member galaxies in each group. This results in $M_{*,3402} = (2.87 \pm 0.43) \times 10^{11} M_\odot$ and $M_{*,5129} = (7.11 \pm 0.95) \times 10^{11} M_\odot$. In addition, we derive the hot gas and stellar masses for our groups out to characteristic radii, r_{500} and r_{200}. For the stellar masses, we simply extended the distance criteria for the group member candidates out to those radii. These quantities, along with other mass components and parameters, are listed in Table 8.

The contribution of cold gas is considerably less than that of the hot gas in these types of systems. Combining this knowledge with the large uncertainties in the other mass components, the effect of the cold, molecular component is negligible here.

5.2. Total Gravitational Mass

Under the assumption of hydrostatic equilibrium, the total mass enclosed within a certain radius (in this case r_{emw}),

$$M_{tot}(< r_{emw}) = \frac{-kT(r)r^2}{G\mu m_p}\left(\frac{\mathrm{d}ln\rho_g(r)}{\mathrm{d}r} + \frac{\mathrm{d}lnT(r)}{\mathrm{d}r}\right), \tag{8}$$

where G is the gravitational constant and the best-fit 3β–Models are used in the first term. Under the assumption of isothermality, the second term in Equation 8 is eliminated and the $T(r)$ in the first term is replaced with the adjusted global temperature given in the Introduction. By observing the temperature profiles, one can see that assuming isothermality is acceptable for NGC 3402. However, this assumption is not valid for NGC 5129, where the profile resembles that of a universal temperature profile. Therefore, we utilized a profile from Sun et al. (2009), specifically Equation 5. Ultimately, we found total dynamical masses within the emission weighted radii of $M_{3402} = (1.16 \pm 0.12) \times 10^{13} M_{\odot}$ and $M_{5129} = (1.69 \pm 0.05) \times 10^{13} M_{\odot}$, which are typical values for poor groups. Furthermore, as for the other mass components, we computed the total enclosed masses out to r_{500} and r_{200} (see Table 8).

6. Discussion

Using *Suzaku* observations of two poor groups, NGC 3402 and NGC 5129, we measure a range of properties of these two groups out to r_{330} and r_{680}, respectively, including the surface brightness, flux, temperature, electron number density, entropy, gravitational mass, and baryon fraction. Thus, we have added NGC 3402 to the rare sample of poor groups with well measured X-ray properties beyond r_{500}.

We first compare the bolometric X-ray luminosities determined in this paper for our groups and their global group temperatures to the L_X–T relations of other works in Figure 10. Plotted are our data and the relations from Xue & Wu (2000), Osmond & Ponman (2004), Dai et al. (2007), Sun (2012) and Bharadwaj et al. (2015), in which we have adjusted the relations to our cosmology. We plotted the Poisson model fit for Dai et al. (2007), the bias corrected group fit for Bharadwaj et al. (2015) and the group relations for the remaining L_X–T relations. The relations chosen were fit based on limited data from galaxy groups, and thus vary widely in slope and normalization. Our data agrees best with the shallow sloped relations by Osmond & Ponman (2004) and Sun (2012), showing no breaks in the L_X–T relation down to temperatures of 0.9 keV. Therefore, X-ray selected (bright) clusters and groups may show universal scaling relations without breaks. Accurate measurements for even lower temperature groups are needed to test if the L_X–T relation breaks at $T \lesssim 0.8$ keV.

The optically selected groups (i.e., Dai et al. 2007), have X-ray luminosities below the L_X–T relations established from the X-ray selected groups (all other relations in Figure 10). Recently, this was independently measured in the group regime (Anderson et al. 2015).

As for the entropy profiles, one can see that the profile for NGC 3402 lies nearly at a constant value above the $r^{1.1}$ self-similar model (Wong et al. 2016), representing the entropy due to purely gravitational processes. On the other hand, the profile for NGC 5129 appears to rapidly converge with the self-similar model at large radii.

We then combined the measurements of the gas, stellar, and gravitational masses, and obtained for the baryon fraction $f_{b,3402} = 0.113 \pm 0.013$ and $f_{b,5129} = 0.091 \pm 0.006$. To compare our data with previous authors' work (Figure 11), we first chose to convert Figure 10 in Dai et al. (2012) from the circular velocity (V_{cir}) at r_{200} to the total gravitational mass enclosed within r_{200} (M_{200}), which provides a more intuitive representation of the physics. Here we used M_{200} described in terms of an average mass density, $\rho_{ave} = 200\rho_{crit}$, where $\rho_{crit} = 3H^2(z)/8\pi G$ is the critical density of the universe and the over-density is a typical value, 200. Since the objects in Figure 11 are relatively low redshift, we used $H(z) \approx H_0$. With this, we rewrote M_{200} in terms of the circular velocity independent of r,

$$M_{200} = \frac{V_{cir}^3}{10H_0G}. \tag{9}$$

For our data, we estimated M_{200} by extrapolating Equation 8 out to r_{200} (as mentioned in §5.2), which we computed from the 3β–Model fit. Then, we compared the stacked and individual clusters and our groups with the M_{200}–T relation in Table 3 from Dai et al. (2007), $M_{200} = Y_0(T/X_0)^k$, where $logY_0 = 13.58 \pm 0.05$, $X_0 = 1$ keV and $k = 1.65 \pm 0.12$. Many systems, including NGC 3402 and NGC 5129, had percent errors from the relation larger than 20%. Thus, for stacked and individual clusters, as well as our data, we used the M_{200}–T relation to compute their M_{200} values. Then, we combined all data and fit with a broken power-law model of the same form as in Dai et al. (2010, 2012),

$$f_b = \frac{0.106(M_{200}/5.40 \times 10^{13}M_\odot)^a}{(1 + (M_{200}/5.40 \times 10^{13}M_\odot)^c)^{b/c}}, \tag{10}$$

where $a = -0.38$, $b = 0.26$ and $c = 2$ (fixed at a smooth break). Above the break, the baryon fraction, f_b, scales as $f_b \propto M_{200}^{a-b=-0.64}$ and $f_b \propto M_{200}^{a=-0.38}$ below the break. Figure 11 depicts the baryon fraction for all systems compiled in Figure 10 of Dai et al. (2012), plus our data with the best fit broken power-law model. Table 8 provides all mass components and baryon fractions for the two groups, as well as their emission weighted radii in familiar over-density forms. Also shown in Table 8 are the values determined for the baryon fractions out to r_{500} and r_{200}, as well as another useful quantity, the gas fraction, f_{gas}. We derived the

gas fraction for our groups out to r_{emw}, r_{500} and r_{200}. The extrapolated baryon fraction out to r_{200} indicates a significant increase towards the cosmic value for both groups. To further analyze this, we extended the model to determine the radii at which we reach the cosmic fraction. For NGC 3402, we were able to find a lower limit on the radius, since the model for the total mass reached a peak at $r = 460$ kpc or an overdensity of $\Delta = 191$. This is a result of the slightly negative β_3 we found for the best-fit model.

Assuming this as a lower limit for the total mass, we find $f_{b3402} \geq f_{cosmic} = 0.175$ at the lower limit of $r = 512$ kpc or $\Delta = 138$. As for NGC 5129, we find that the baryon fraction never reaches cosmic, maxing out at $r = 752$ kpc or $\Delta = 81$. These findings strongly imply that much of the expected baryon content lies well outside the virial radii for these groups.

To glean a further understanding of the baryon fractions of galaxy groups with low temperatures ($T \lesssim 1.3$ keV) and measured at large radii, we combined our data with that of a previous work. There are three other groups, all from Sun et al. (2009), whose adjusted temperatures are measured out to a large fraction of r_{500}. Listed in Table 9 are the f_b, global T and measurement radii, where we symmetrized their uncertainties. Then, we plotted these groups with NGC 3402 and NGC 5129 and computed the Bayesian average, $f_{b,ave} = 0.100 \pm 0.004$, which is shown in the solid blue region of Figure 12. The averaged f_b falls significantly below the cosmological value for $\Omega_m = 0.26$ and $\Omega_\Lambda = 0.74$, $f_{b,CMB} = 0.175 \pm 0.012$[1]. We conclude that, on average, significant baryon deficits exist for poor groups with temperatures between 0.8–1.3 keV. Other recent studies also found deficits of baryons in galaxy groups, although at higher temperatures of 2–3 keV (Sanderson et al. 2013; Laganá et al. 2013). These results reinforce our conclusion that it is in the galaxy group regime that baryon deficits become significant.

We thank E. O'Sullivan for providing the updated *XMM-Newton* and *Chandra* inner temperature profile of NGC 3402 and for his helpful comments. This research has made use of the NASA/IPAC Extragalactic Database (NED), which is operated by the Jet Propulsion Laboratory, California Institute of Technology, under contract with the National Aeronautics and Space Administration. In addition, this research has utilized data, software and/or web tools obtained from NASA's High Energy Astrophysics Science Archive Research Center (HEASARC), a service of Goddard Space Flight Center and the Smithsonian Astrophysical Observatory. Also, we acknowledge support for this work from the NASA grants NNX11AG96G, NNX11AD09G, and the NSF grant AST-1413056. This research has made use of data obtained from the *Suzaku* satellite, a collaborative mission between the space

[1]For WMAP-7 cosmology, $f_{b,CMB} = 0.169 \pm 0.008$ (Jarosik et al. 2011).

agencies of Japan (JAXA) and the USA (NASA).

REFERENCES

Akamatsu, H., Hoshino, A., Ishisaki, Y., et al. 2011, PASJ, 63, 1019

Anders, E., & Grevesse, N. 1989, Geochim. Cosmochim. Acta, 53, 197

Anderson, M. E., & Bregman, J. N. 2011, ApJ, 737, 22

Anderson, M. E., Gaspari, M., White, S. D. M., Wang, W., & Dai, X. 2015, MNRAS, 449, 3806

Arnaud, M. 2005, Background Microwave Radiation and Intracluster Cosmology, 77

Bautz, M. W., Miller, E. D., Sanders, J. S., et al. 2009, PASJ, 61, 1117

Bell, E. F., & de Jong, R. S. 2001, ApJ, 550, 212

Bell, E. F., McIntosh, D. H., Katz, N., & Weinberg, M. D. 2003, ApJS, 149, 289

Benson, A. J. 2010, Phys. Rep., 495, 33

Bharadwaj, V., Reiprich, T. H., Lovisari, L., & Eckmiller, H. J. 2015, A&A, 573, A75

Bregman, J. N. 2007, ARA&A, 45, 221

Bristow, P. D., & Phillipps, S. 1994, MNRAS, 267, 13

Bryan, G. L., & Norman, M. L. 1998, ApJ, 495, 80

Crook, A. C., Huchra, J. P., Martimbeau, N., et al. 2007, ApJ, 655, 790

Dai, X., Kochanek, C. S., & Morgan, N. D. 2007, ApJ, 658, 917

Dai, X., Bregman, J. N., Kochanek, C. S., & Rasia, E. 2010, ApJ, 719, 119

Dai, X., Anderson, M. E., Bregman, J. N., & Miller, J. M. 2012, ApJ, 755, 107

Eckert, D., Vazza, F., Ettori, S., et al. 2012, A&A, 541, A57

Eckmiller, H. J., Hudson, D. S., & Reiprich, T. H. 2011, A&A, 535, A105

Flynn, C., Holmberg, J., Portinari, L., Fuchs, B., & Jahreiß, H. 2006, MNRAS, 372, 1149

Fujita, Y., Tawa, N., Hayashida, K., et al. 2008, PASJ, 60, 343

Fujimoto, R., Mitsuda, K., Mccammon, D., et al. 2007, PASJ, 59, 133

Fukugita, M., Hogan, C. J., & Peebles, P. J. E. 1998, ApJ, 503, 518

Gastaldello, F., Buote, D. A., Humphrey, P. J., et al. 2007, ApJ, 669, 158

Gavazzi, R., Treu, T., Rhodes, J. D., et al. 2007, ApJ, 667, 176

George, M. R., Fabian, A. C., Sanders, J. S., Young, A. J., & Russell, H. R. 2009, MNRAS, 395, 657

Guzzo, L., Schuecker, P., Böhringer, H., et al. 2009, A&A, 499, 357

Hoshino, A., Henry, J. P., Sato, K., et al. 2010, PASJ, 62, 371

Humphrey, P. J., & Buote, D. A. 2006, ApJ, 639, 136

Humphrey, P. J., Buote, D. A., Canizares, C. R., Fabian, A. C., & Miller, J. M. 2011, ApJ, 729, 53

Humphrey, P. J., Buote, D. A., Brighenti, F., et al. 2012, ApJ, 748, 11

Ichikawa, K., Matsushita, K., Okabe, N., et al. 2013, ApJ, 766, 90

Jarosik, N., Bennett, C. L., Dunkley, J., et al. 2011, ApJS, 192, 14

Johnson, R., Finoguenov, A., Ponman, T. J., Rasmussen, J., & Sanderson, A. J. R. 2011, MNRAS, 413, 2467

Kawaharada, M., Okabe, N., Umetsu, K., et al. 2010, ApJ, 714, 423

Laganá, T. F., Martinet, N., Durret, F., et al. 2013, A&A, 555, AA66

Mahdavi, A., & Geller, M. J. 2004, ApJ, 607, 202

Mahdavi, A., Finoguenov, A., Böhringer, H., Geller, M. J., & Henry, J. P. 2005, ApJ, 622, 187

McGaugh, S. S. 2005, ApJ, 632, 859

Mulchaey, J. S. 2000, ARA&A, 38, 289

Osmond, J. P. F., & Ponman, T. J. 2004, MNRAS, 350, 1511

O'Sullivan, E., Vrtilek, J. M., Harris, D. E., & Ponman, T. J. 2007, ApJ, 658, 299

Persic, M., & Salucci, P. 1992, MNRAS, 258, 14P

Reiprich, T. H., Hudson, D. S., Zhang, Y.-Y., et al. 2009, A&A, 501, 899

Rykoff, E. S., Evrard, A. E., McKay, T. A., et al. 2008, MNRAS, 387, L28

Sanderson, A. J. R., O'Sullivan, E., Ponman, T. J., et al. 2013, MNRAS, 429, 3288

Sato, T., Sasaki, T., Matsushita, K., et al. 2012, PASJ, 64, 95

Sakamoto, T., Chiba, M., & Beers, T. C. 2003, A&A, 397, 899

Shen, S., Kauffmann, G., von der Linden, A., White, S. D. M., & Best, P. N. 2008, MNRAS, 389, 1074

Simionescu, A., Allen, S. W., Mantz, A., et al. 2011, Science, 331, 1576

Stark, D. V., McGaugh, S. S., & Swaters, R. A. 2009, AJ, 138, 392

Sun, M., Voit, G. M., Donahue, M., et al. 2009, ApJ, 693, 1142

Sun, M. 2012, New Journal of Physics, 14, 045004

Vikhlinin, A., Markevitch, M., Murray, S. S., et al. 2005, ApJ, 628, 655

Vikhlinin, A., Kravtsov, A., Forman, W., et al. 2006, ApJ, 640, 691

Walker, M. G., Mateo, M., Olszewski, E. W., et al. 2007, ApJ, 667, L53

Walker, S. A., Fabian, A. C., Sanders, J. S., & George, M. R. 2012, MNRAS, 424, 1826

Wong, K.-W., Irwin, J. A., Wik, D. R., et al. 2016, ApJ, 829, 49

Xue, Y.-J., & Wu, X.-P. 2000, ApJ, 538, 65

Yamaguchi, H., Nakajima, H., Koyama, K., et al. 2006, Proc. SPIE, 6266, 121

This preprint was prepared with the AAS LaTeX macros v5.2.

Table 1. Observation Parameters

Observation	Obs. ID	Date	RA(J2000) deg	Dec (J2000) deg	Raw/Final Exposure Time(ks)[a] XIS0	XIS1	XIS3
NGC3402	805070010	2010/12/27	162.4923	−13.1954	49.4/24.1	49.2/24.2	49.4/24.2
NGC3402back	805071010	2010/12/19	161.6656	−13.5535	15.2/12.5	15.1/12.5	15.3/12.5
NGC5129 1st	805072010	2010/12/18	201.3141	14.0346	55.4/25.6	53.5/25.6	55.8/25.6
NGC5129 2nd	805073010	2010/12/18	201.1253	13.7341	37.9/25.4	37.7/25.3	37.9/25.4
NGC5129back	805074010	2010/12/17	201.7433	13.5725	16.4/12.3	15.8/12.3	16.5/12.3

[a]Final exposure times after all screening, including the COR2 > 6 GV condition.

Table 2. Mean Surface Brightnesses and Number Densities at r_{emw}

Observation	FI (XIS0,XIS3)/BI	Direct Subtraction S (10^{-8} cts s^{-1} kpc^{-2})[a]	Spectral Analysis S (10^{-8} cts s^{-1} kpc^{-2})[a]	n_e (10^{-5} cm^{-3})
NGC3402	FI	1.7 ± 1.9, 0.5 ± 1.8	7.0 ± 0.5	9.5 ± 8.0
NGC3402	BI	1.0 ± 2.3	11.7 ± 0.9	8.8 ± 7.4
NGC5129 1st	FI	−1.5 ± 1.2, 0.1 ± 1.1	1.6 ± 0.4	7.8 ± 3.0
NGC5129 1st	BI	0.5 ± 1.6	2.8 ± 0.6	7.3 ± 2.8
NGC5129 2nd	FI	−1.9 ± 1.3, -0.3 ± 1.1	2.7 ± 1.0	11.5 ± 6.0
NGC5129 2nd	BI	−1.5 ± 1.6	6.6 ± 2.5	10.7 ± 5.5

[a]Note the effective areas of the CCDs have not been divided, since they are energy dependent.

Table 3. Emission Line Energies of the Non-X-ray Background

Element	Transition	Energy (keV)
Al	Kα	1.486
Si	Kα	1.740
Au	Kα	2.123
Mn	Kα	5.895
Mn	Kβ	6.490
Ni	Kα	7.470

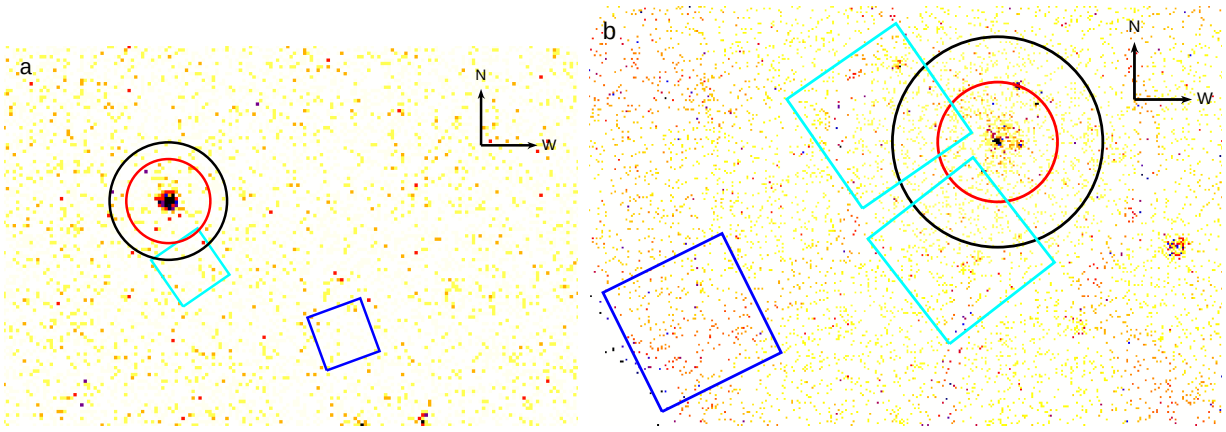

Fig. 1.— ROSAT images for (*a*) NGC 3402 and (*b*) NGC 5129 with overlaid extent of the Chandra spectral analysis from Sun et al. (2009) (red circles), extent of r_{500} according to our electron number density profile (black circles), the *Suzaku* FOV for observations of the two groups (cyan squares) and their corresponding *Suzaku* background observations (blue squares).

Table 4. Xspec Background Parameters and Normalizations for Spectral Analysis

Emission Source	Model Type	Parameter	Fixed/Free	NGC 3402	NGC 5129
Galactic Absorption	wabs	$N_H(10^{22}$ cm$^{-2})$	Fixed	0.0477	0.0178
AGN	power-law	Γ	Fixed	1.41	1.41
		Normalization (cm^{-5})	Free	$(8.5 \pm 0.3) \times 10^{-4}$	$(1.18 \pm 0.04) \times 10^{-3}$
Galaxy	apec	kT (keV)	Fixed	0.07	0.07
		Abundance (Z$_\odot$)	Fixed	1	1
		Redshift	Fixed	0	0
		Normalization	Free	0.043 ± 0.013	$0.012\ ^{+0.020}_{-0.012}$
Galaxy	apec	kT	Fixed	0.2	0.2
		Abundance	Fixed	1	1
		Redshift	Fixed	0	0
		Normalization	Free	$(1.2 \pm 0.2) \times 10^{-3}$	$(3.5 \pm 0.5) \times 10^{-3}$
Galaxy	apec	kT	Fixed	···	0.4
		Abundance	Fixed	···	1
		Redshift	Fixed	···	0
		Normalization	Free	···	$(4.8 \pm 1.2) \times 10^{-4}$
		χ^2_{min}/dof		120/123	187/172
		χ^2_ν range[a]		0.964–1.01	1.08–1.10

[a]Range in reduced χ^2 for the eight different background models.

Table 5. Xspec Group Parameters and Normalizations for Spectral Analysis

Emission Source	Model Type	Parameter	Fixed/Free	NGC 3402	NGC 5129 1st; NGC 5129 2nd
Galactic Absorption	wabs	$N_H(10^{22}$ cm$^{-2})$	Fixed	0.046	0.0176; 0.0177
Group Hot Halo	apec	kT (keV)	Free	$1.01 \pm 0.05^{a} \pm 0.01^{b}$	$0.862\ ^{+0.067}_{-0.045}{}^{a} \pm 0.002^{b}$; $0.72\ ^{+0.17}_{-0.05}{}^{a} \pm 0.02^{b}$
		Abundance ($Z_\odot$)	Fixed	0.2	0.2
		Redshift	Fixed	0.0153	0.0230
		Normalization	Free	$(2.01 \pm 0.15^{a} \pm 0.07^{b})\times10^{-3}$	$(5.7\ ^{+1.0}_{-1.6}{}^{a} \pm 0.7^{b})\times10^{-4}$; $(1.1\ ^{+0.3}_{-0.5}{}^{a} \pm 0.2^{b})\times10^{-3}$
		χ^2_{min}/dof		188/194	349/339; 270/255
		χ^2_ν range[c]		0.954–1.07	1.01–1.05; 1.06–1.08

[a]Statistical uncertainties

[b]Systematic uncertainties based on the eight different background models.

[c]Same as in Table 4.

Table 6. 2β–Model Fit Parameters

Model Parameters	Value (inner)	
	NGC 3402	NGC 5129
r_{c1}(kpc)	95 ± 14	74 ± 5
β_1	1.2 ± 0.3	0.57 ± 0.03
$n_{e01}(\mathrm{cm}^{-3})$	$(1.1 \pm 0.13) \times 10^{-3}$	$(1.1 \pm 0.1) \times 10^{-3}$
r_{c2}(kpc)	2.4 ± 0.2	0.041[a]
β_2	0.52 ± 0.02	0.55 ± 0.02
$n_{e02}(\mathrm{cm}^{-3})$	0.12 ± 0.01	37[a]
χ^2_{min}/dof	57.9/58	45.8/46

Note. — Best fit parameters for the 2β–Model considering only inner data. Clearly, the inner data are well represented by two β models.

[a]r_{c2} and n_{e02} are highly correlated for NGC 5129, thus we chose not to consider uncertainties for these parameters.

Table 7. 3β–Model Fit Parameters

Model Parameters	Value (inner plus our data)	
	NGC 3402	NGC 5129
r_{c1}(kpc)	121 ± 11	80.5 ± 3.8
β_1	1.78 ± 0.23	0.641 ± 0.039
$n_{e01}(\mathrm{cm}^{-3})$	$(1.07 \pm 0.04) \times 10^{-3}$	$(1.07 \pm 0.04) \times 10^{-3}$
r_{c2}(kpc)	2.48 ± 0.12	0.041 ± 0.003
β_2	0.519 ± 0.006	0.548 ± 0.008
$n_{e02}(\mathrm{cm}^{-3})$	0.113 ± 0.006	36.9 ± 3.0
r_{c3}(kpc)	200[a]	200[a]
β_3	−0.009 ± 0.042	0.010 ± 0.089
$n_{e03}(\mathrm{cm}^{-3})$	$(3.33 \pm 0.93) \times 10^{-5}$	$(2.05 \pm 1.22) \times 10^{-5}$
σ_{ne}/n_e (%)	26%	22.9% (1^{st} obs.), 27.1% (2^{nd} obs.)
χ^2_{min}/dof	47.9/58	45.8/48

Note. — Best fit parameters for the 3β–Model with both inner and outer data and prior terms in the χ^2.

[a]r_{c3} was chosen to be fixed in all fits.

Table 8. Derived Group Properties

Property	NGC 3402	NGC 5129
$M_{*,emw}$ $(10^{11} M_\odot)$	2.87 ± 0.43	7.11 ± 0.95
$M_{g,emw}(10^{11} M_\odot)$	10.3 ± 0.3	8.28 ± 0.11
$M_{emw}(10^{13} M_\odot)$	1.16 ± 0.12	1.69 ± 0.05
$M_{500}(10^{13} M_\odot)$	1.15	1.85
$M_{200,M-T}$[a] $(10^{13} M_\odot)$	2.95	3.06
$M_{200}(10^{13} M_\odot)$	1.164	2.38
$f_{g,emw}$	0.089 ± 0.010	0.049 ± 0.002
$f_{g,500}$	0.072	0.056
$f_{g,200}$	0.117	0.079
$f_{b,emw}$	0.113 ± 0.013	0.091 ± 0.006
$f_{b,500}$	0.097	0.096
$f_{b,200}$	0.146	0.123
r_{emw}(kpc)[b]	383	329
Δ[c]	330	680
r_{500}(kpc)	333	376
r_{200}(kpc)	453	544
$L_{X,bol,emw}(10^{42}$ erg s$^{-1})$	14.3 ± 0.3	5.40 ± 0.17
$L_{X,bol,500}(10^{42}$ erg s$^{-1})$	14.1 ± 0.3	5.46 ± 0.17
$L_{X,bol,200}(10^{42}$ erg s$^{-1})$	14.5 ± 0.3	5.70 ± 0.18
$L_{ROSAT}(10^{42}$ erg s$^{-1})$	13.8 ± 0.3	5.20 ± 0.16
$F_X(10^{-12}$ erg cm^{-2} s$^{-1})$	18.5 ± 0.4	3.06 ± 0.09

Note. — M_{emw} is the total gravitational mass (based on the Hydrostatic equation) enclosed by r_{emw}. All quantities derived are based on $h = 0.73$ and are related to the Hubble constant by $M_* \propto h^{-2}$, $M_g \propto h^{-5/2}$, $M_{emw} \propto h^{-1}$ and $r \propto h^{-1}$.

[a]This value for M_{200} was derived from the Poisson fit to the M_{200}–T relation in Dai et al. (2007).

[b]The r_{emw} here is the emission weighted observation radius for each galaxy group.

[c]Δ is the constant term which, when multiplied by ρ_{crit}, gives the average mass density of the group.

Table 9. Sun et al. (2009) Groups and Properties

Galaxy Group	r/r_{500}	f_b	kT (keV)
NGC 1550	0.76	0.113 ± 0.011	1.26 ± 0.02
NGC 5098	1.06	0.190 ± 0.024	1.14 ± 0.05
UGC 5088	0.87	0.085 ± 0.013	0.96 ± 0.04

Note. — Properties of the groups measured out to or near r_{500} in Sun et al. (2009) groups, adjusted for the change in AtomDB.

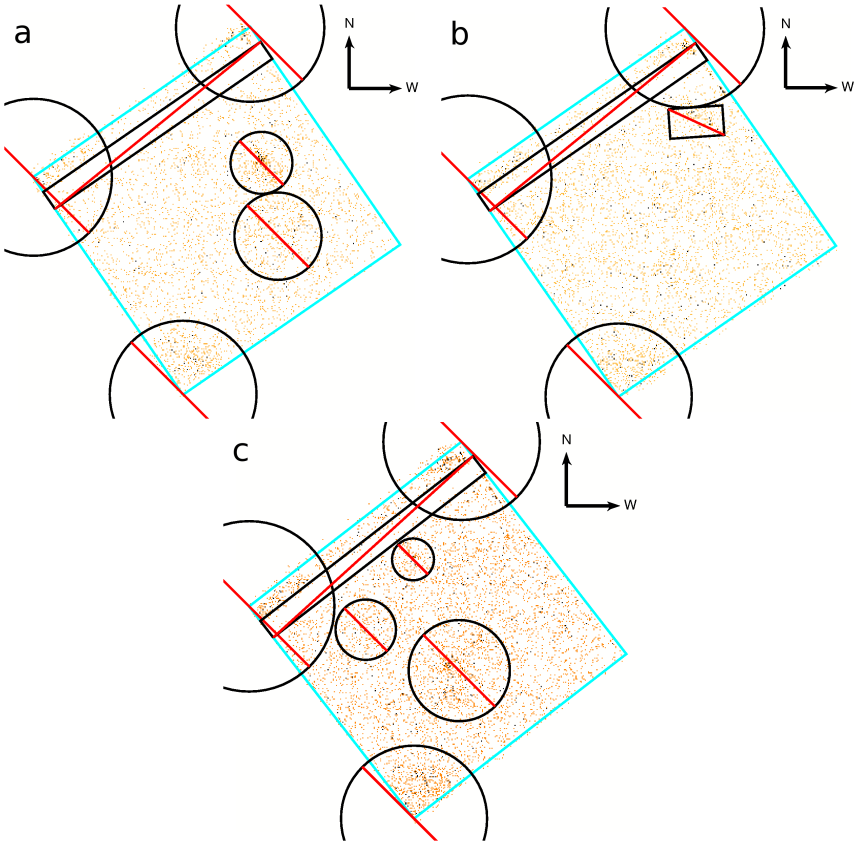

Fig. 2.— (a) NGC 3402, (b) NGC 5129 1st and (c) 2nd XIS0 3x3 formatted images with inclusion, exclusion regions and the COR2 $>$ 6 GV condition. The method for determination of regions is discussed in Section 2.

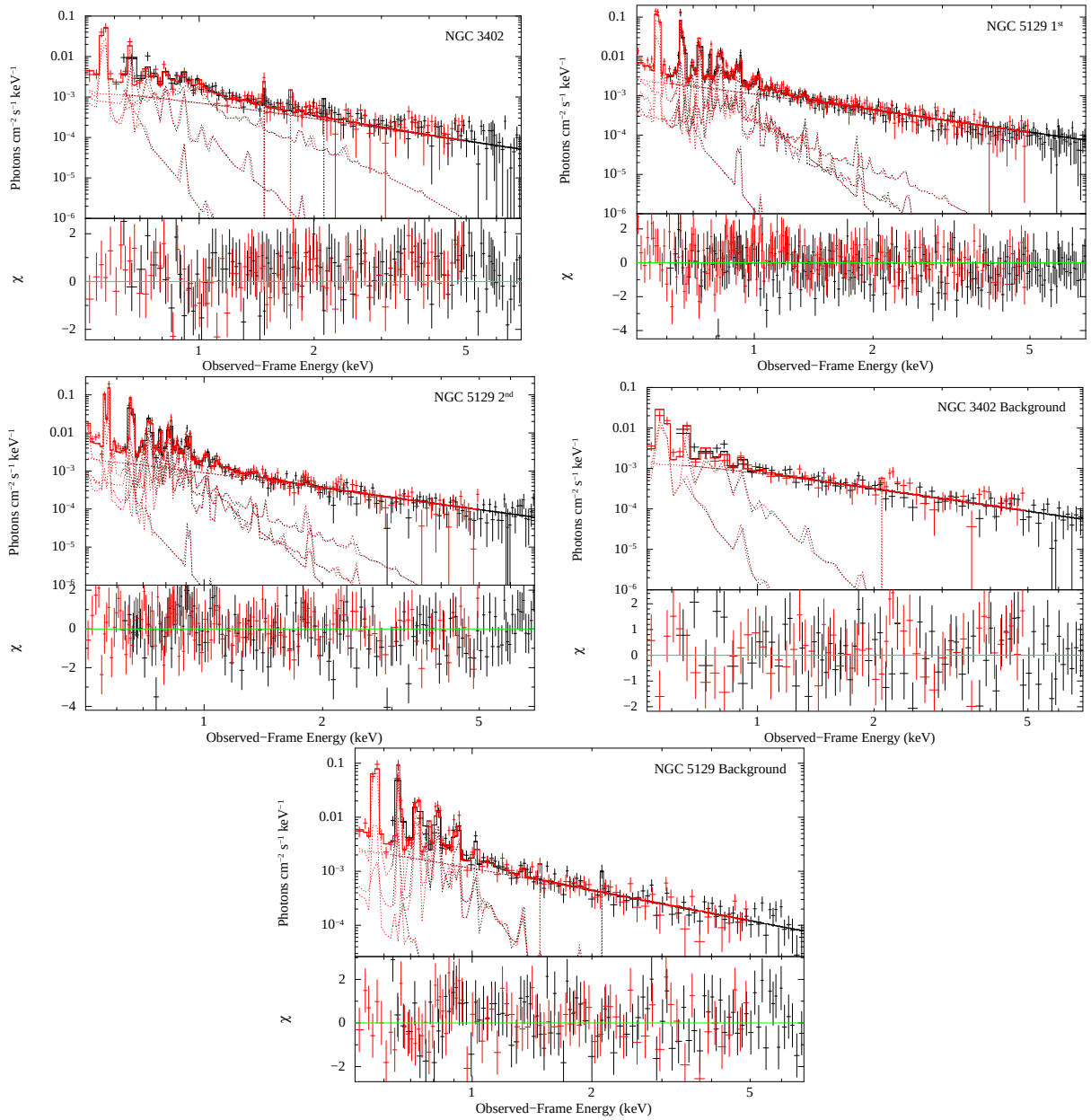

Fig. 3.— Unfolded spectra for NGC 3402 and NGC 5129 off-axis observations, as well as spectra of background pointings. The solid lines are the best fit theoretical model, not folded with the instrument response, while the crosses are the corresponding binned spectral data. Black denotes FI CCDs, whereas red represents the BI CCD. Bottom panel in each image are the residuals in units of standard deviation with error bars of 1σ.

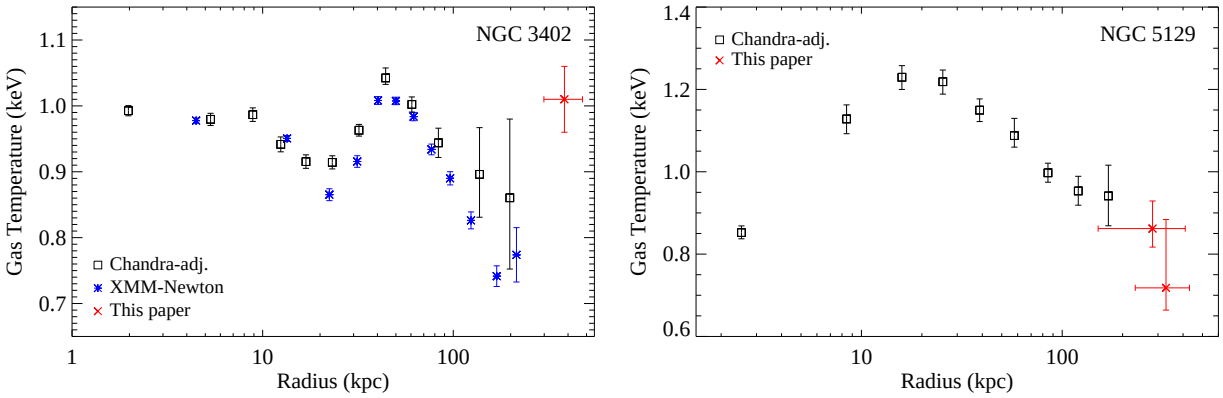

Fig. 4.— Temperature profiles with 1σ uncertainties in temperature and emission weighted radial binsizes, as discussed in Section 4.3. Black squares are projected *Chandra* data retrieved from Sun et al. (2009) and adjusted to AtomDB ver. 2.0.2, blue asterisks are projected XMM-Newton data (O'Sullivan, private communication) and red crosses are the data from this paper.

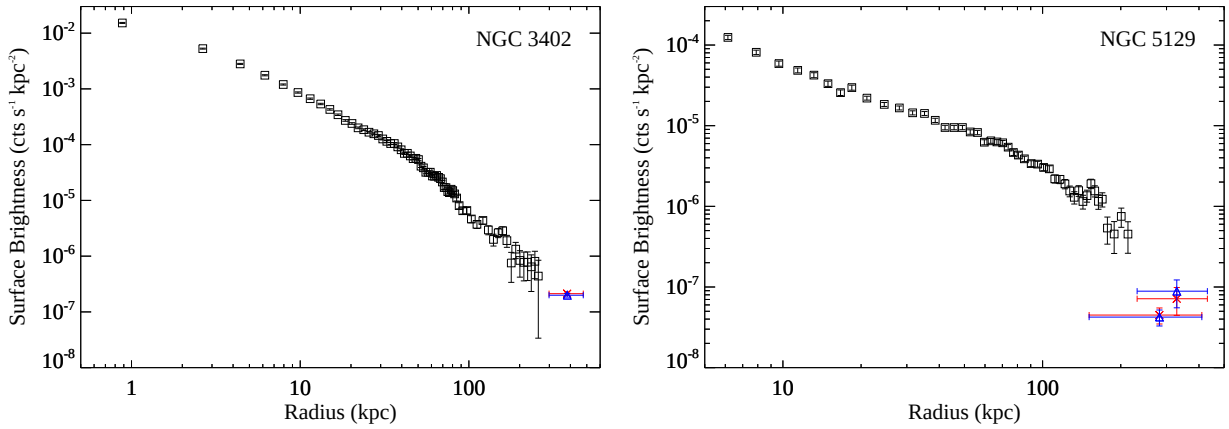

Fig. 5.— Mean surface brightness profiles with 1σ uncertainties in SB and emission weighted radial binsizes, as discussed in Section 4.4. Black squares are *Chandra* data, while red crosses and blue triangles are the FI and BI data from this work, respectively. Note the surface brightness has not been divided by the effective area of the telescope, which is energy dependent.

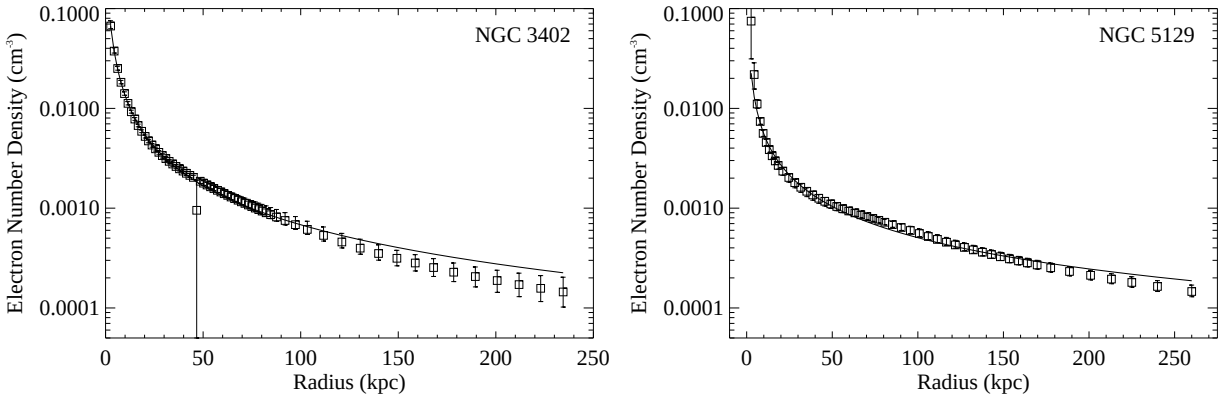

Fig. 6.— Single β–Model fits (black lines) to the *Chandra* data from Sun et al. (2009).

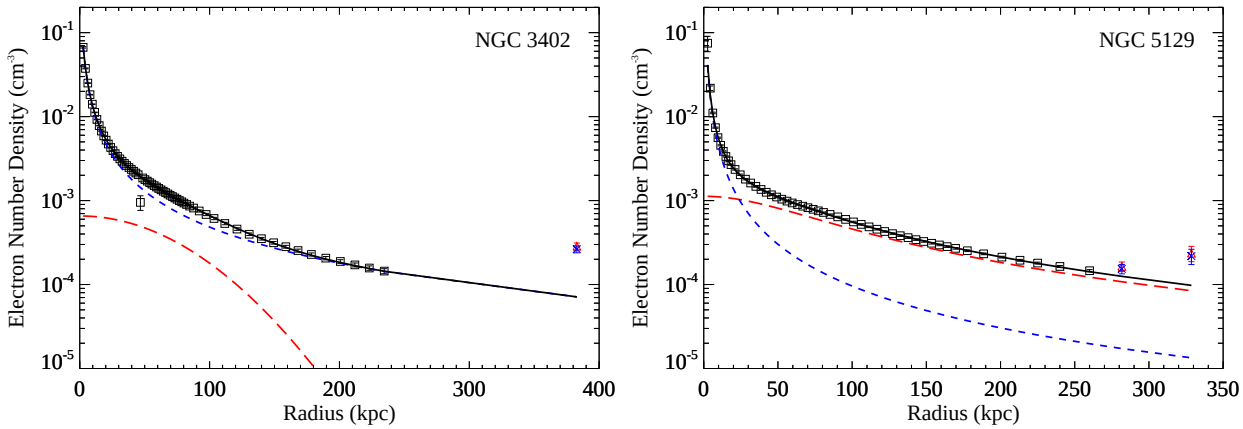

Fig. 7.— 2β–Model fits to the *Chandra* data plus the data added in this paper. The uncertainties are those with the adjustments mentioned in Section 4.5. Red and blue dashed lines are the first and second β model components, respectively, while the black is the sum of the two. Black squares, red crosses and blue triangles have the same meaning as in Figure 5.

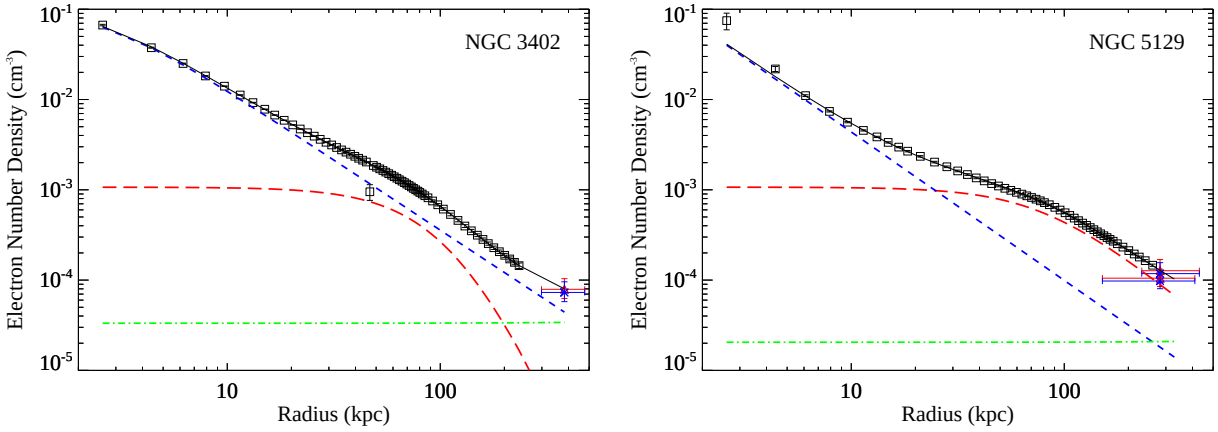

Fig. 8.— 3β–Model fits to the *Chandra* data plus data from this work. Uncertainties in the outer data are from the uncertainty estimation described in § 4.5., while uncertainties in the inner data are the same as in the 2β models. Red and blue dashed lines represent the first and second β models, whereas the green dashed line is the third β model component. As in Figure 7, the solid black line is the sum of all three models. Black squares, red crosses and blue triangles have the same meaning as in Figure 5.

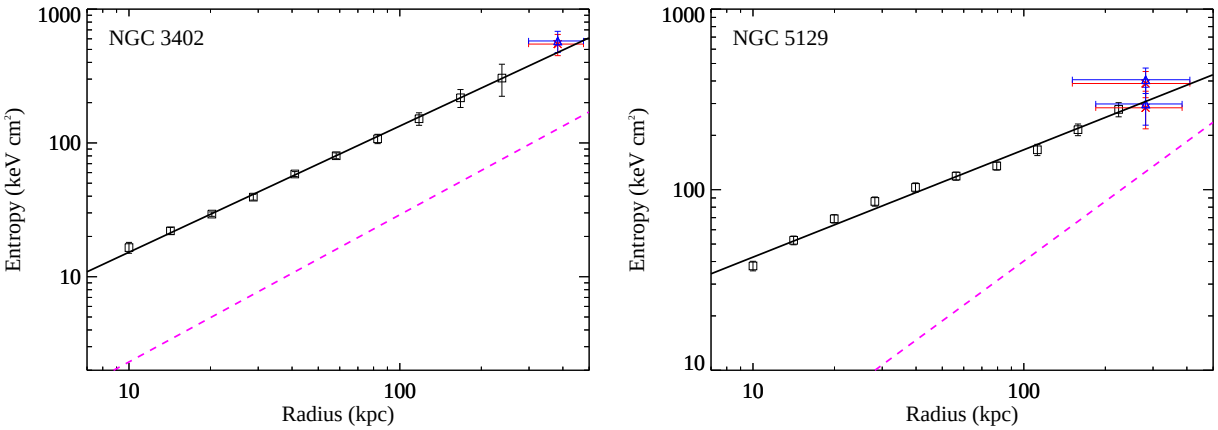

Fig. 9.— Entropy profiles of NGC 3402 and NGC 5129 groups, where black squares are Chandra data from Sun et al. (2009), adjusted to the recent version of AtomDB and red crosses and blue triangles have the same meaning as in Figure 5. The solid black lines are power-law fits to the data, whereas the dashed magenta lines are the self-similar models as discussed in § 4.6.

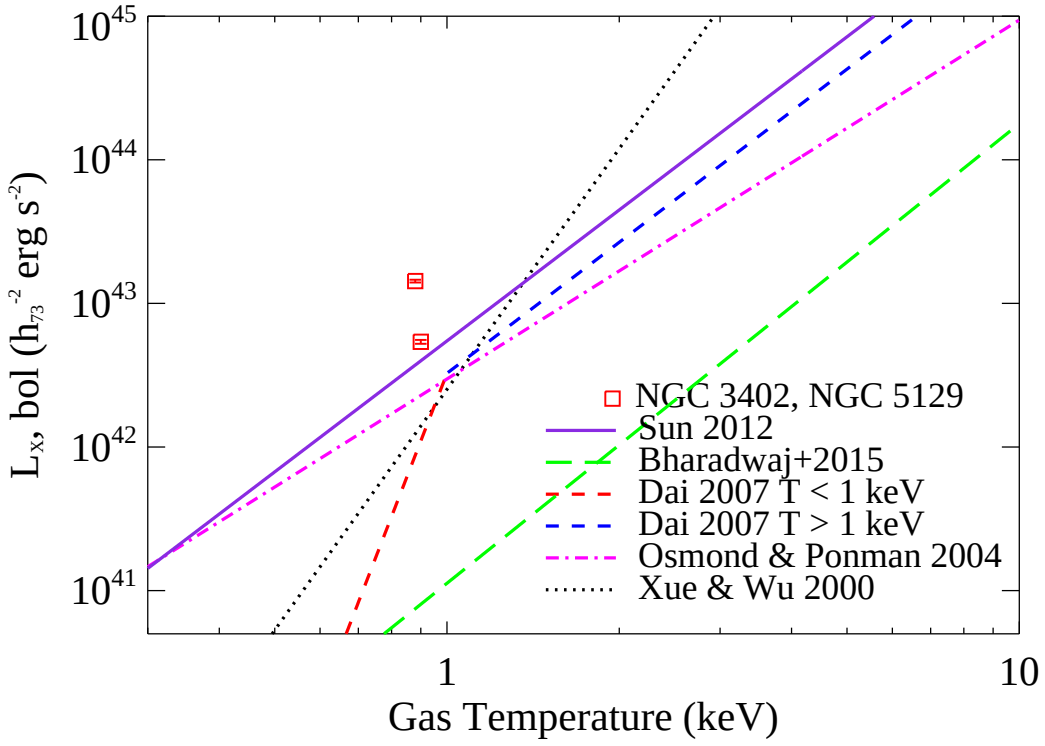

Fig. 10.— Bolometric X–ray luminosity (0.1–100 keV) plotted versus global gas temperature for NGC 3402 and NGC 5129. Also plotted are various L_X–T relations from the literature, corrected for cosmology.

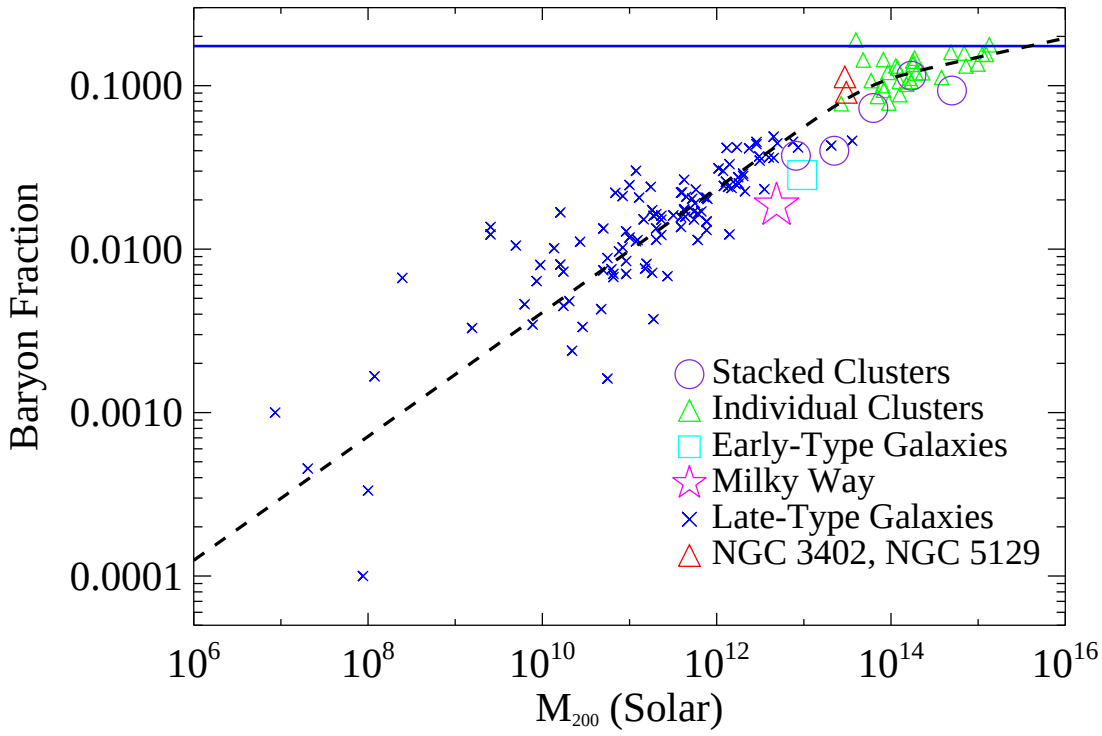

Fig. 11.— Baryon fraction as a function of M_{200}, or mass enclosed by r_{200}. Plotted are the measurements from Sakamoto et al. (2003), McGaugh (2005), Flynn et al. (2006), Vikhlinin et al. (2006), Gavazzi et al. (2007), Walker et al. (2007), Stark et al. (2009), Sun et al. (2009), Dai et al. (2010), Anderson & Bregman (2011) and this work, converted from circular velocity to M_{200}. The blue solid line is the cosmological baryon fraction measured from the CMB, and the black dashed line is the best-fit broken power-law model for baryon losses.

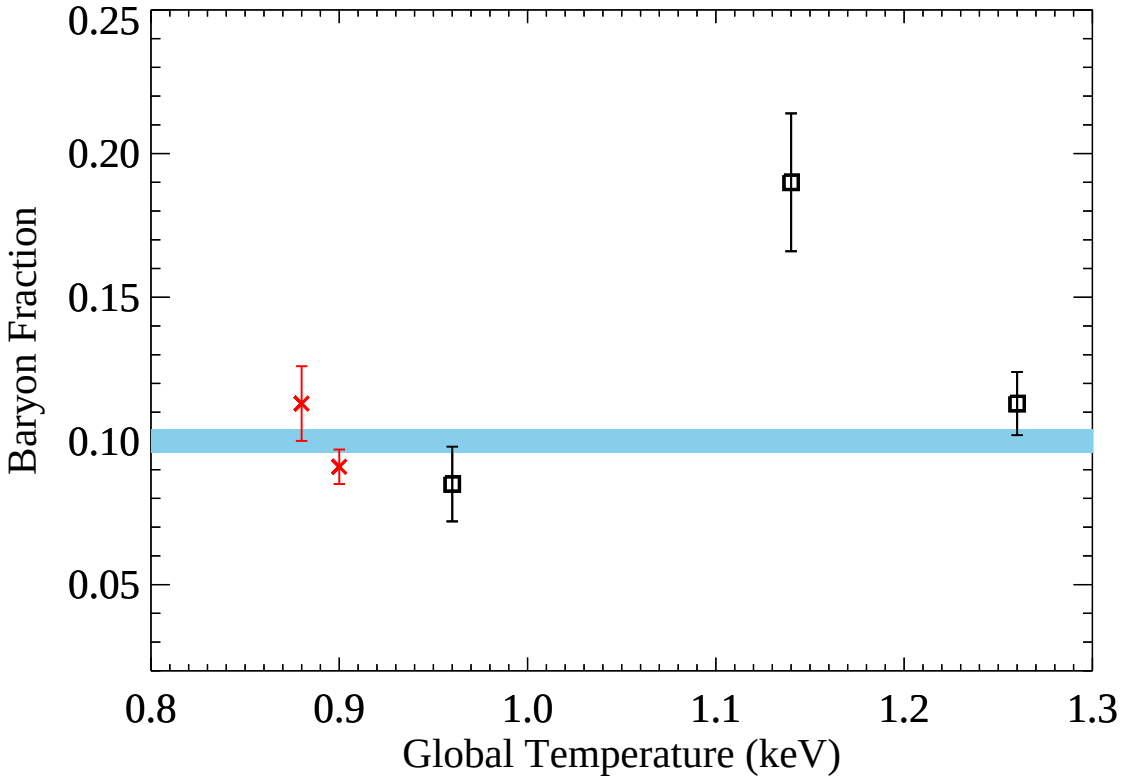

Fig. 12.— Baryon fraction versus temperature plotted for 5 galaxy groups with hot gas temperatures less than 1.3 keV and whose baryon fractions were determined within $r \geq 0.76 r_{500}$ (black squares). The solid blue region is the Bayesian averaged f_b and 1σ uncertainy, whereas the red crosses are the results from this paper

.